NISTIR 8300

Improving 3D Vision-Robot Registration for Assembly Tasks

Marek Franaszek
Geraldine S. Cheok
Karl van Wyk
Jeremy A. Marvel

This publication is available free of charge from:
https://doi.org/10.6028/NIST.IR.8300

National Institute of Standards and Technology
U.S. Department of Commerce

NISTIR 8300

Improving 3D Vision-Robot Registration for Assembly Tasks

Marek Franaszek
Geraldine S. Cheok
Jeremy A. Marvel
Engineering Laboratory
National Institute of Standards and Technology

Karl van Wyk
Nvidia

This publication is available free of charge from:
https://doi.org/10.6028/NIST.IR.8300

April 2020

U.S. Department of Commerce
Wilbur L. Ross, Jr., Secretary

National Institute of Standards and Technology
Walter Copan, NIST Director and Undersecretary of Commerce for Standards and Technology

National Institute of Standards and Technology Interagency or Internal Report 8300
Natl. Inst. Stand. Technol. Interag. Intern. Rep. 8300, 32 pages (April 2020)

This publication is available free of charge from:
https://doi.org/10.6028/NIST.IR.8300

Abstract

Good registration between the coordinate frames of a perception system and a robot is important for the efficient operation of autonomous systems in vision-guided assembly lines. Rigid-body registration, which is based on the measurement of corresponding points (fiducials) in both frames, is a commonly used method. Noise and possible bias in the measured points degrade the quality of registration as gauged by the Target Registration Error (*TRE*). A method to restore the rigid body condition (RRBC) was recently developed to reduce *TRE* when the bias is larger than the noise. This was achieved by applying corrections to target locations in the vision sensor frame. This paper presents two procedures to improve the performance of the RRBC method by: 1) selecting the location of fiducials used for calculating correction to the target location and 2) selecting the correct arm configuration for fiducial from multiple configurations as calculated by inverse kinematics. Experiments performed with a motion tracking system and two different robot arms show that these two procedures can further reduce the Root Mean Square of *TRE* (RMS_T) to less than 20 % of the uncorrected RMS_T.

Key words

inverse kinematics; peg-in-hole test; rigid body registration; target registration error; volumetric error compensation.

Table of Contents

List of Tables

List of Figures

1. INTRODUCTION

Different manufacturing tasks performed by autonomous systems require accurate transformation between the coordinate frames of the vision system and the robot. An inaccurate transformation causes misalignment between parts, which negatively impacts the performance of assembly tasks [1]. The same is also true for other tasks, such as automated drilling [2] or welding [3], where accurate positioning is critical. Inspections of large parts (e.g., on the order of meters), such as wind turbine blades [4] or components of an airplane [5-7], are frequently performed by sensors mounted on a robot arm [8, 9], but the required tolerances are submillimeter. Due to the size of the scanned parts, multiple scans from different viewpoints are often required. These scans must then be merged together to generate a full three-dimensional (3D) model of the as-built part for comparison with the Computer Aided Design (CAD) model to determine any discrepancies. Since these discrepancies consist of both machining errors and registration errors, an accurate transformation between the world frame (where inspected part is located) and the robot frame is critical.

There are various methods available to determine the transformation between coordinate frames. Point-based, rigid-body registration is a commonly used method, and it assumes that the same set of points (called fiducials) can be measured in both frames. When the location of a point in the robot frame cannot be fully determined from forward kinematics alone due to an unknown offset between the end of the arm and the Tool Center Point (TCP), then more general hand-eye (robot-sensor) calibration techniques must be used [10]. In this study, this offset was known, and the points measured by the perception system could be determined in the robot frame allowing the use of point-based registration. However, noise and possible bias in the measured points introduce error into the registration process. This error is propagated when transforming target points $\boldsymbol{T}_X$ from sensor to robot frame (target points are points which are measured only in the perception system frame but must be accessed in the robot frame).

To reduce Target Registration Error (*TRE*), a method was proposed in [11] called the Restoration of Rigid Body Condition (RRBC). In this method, small corrections to measured fiducial locations were calculated, and these corrections were then used to estimate a correction to any target point $\boldsymbol{T}_X$ via linear interpolation.

Since the RRBC utilizes a linear interpolation scheme, its performance depends on how well the unknown registration error is approximated by linear interpolation in Cartesian space. This is an important issue in robotics because two 3D points (TCPs) close to each other in Cartesian space may have corresponding arm configurations with very different sets of joint angles. When a robot's forward kinematic model has inaccurate parameters (e.g., joint angle offsets) then the registration error becomes discontinuous. This adversely impacts both the analytical modeling techniques and the interpolation schemes.

In this paper, we investigate how the performance of the RRBC method can be enhanced by selection of the: 1) distance between a target and its nearest fiducials from which the corrections are interpolated, and 2) the robot arm configuration for those fiducials. We show that the accuracy of the correction to the target location increases with decreasing distance which results in reduced *TRE*. Improvement in the performance of the RRBC can also be observed when fiducials closest to the target (in Cartesian space) have joint configurations close to the arm configuration for the target. Based on these observations, we propose a

procedure to judiciously select fiducial locations which maximizes the reduction of target registration error while limiting the amount of acquired data necessary for the enhanced RRBC method.

2. RELATED WORK

A method of correcting positional error very similar to RRBC was proposed by Zeng et al. for a robotic drilling and riveting system [12]. They estimated positional error using linear regression in the space of joint angles to model robot kinematic error and Gaussian noise to model non-kinematic errors, such as joint compliance, friction, backlash and thermal effect. The parameters of the model were obtained from measurements of 100 points randomly distributed in a (1.2 ×1.2 ×1.2) m work volume. The corrections evaluated from the global model were calculated for another set of 100 random points which served as target points for testing the procedure. Using a laser tracker, they reduced the maximum positional errors of a KUKA KR 500-3 by 84.04 %, from 2.01 mm to 0.32 mm. Similar to the RRBC, their method does not require access to the internal robot parameters as it merely modifies location of the commanded point.

For assemblies involving flexible parts and components, the rigid-body condition is effectively negated, and non-rigid registration methods have to be used [13]. This is common in the field of medical imaging where many parts of the human body cannot be considered as rigid objects [14, 15]. Fortunately, deviations from the rigid-body condition in manufacturing are frequently smaller than in medical applications, and other methods can be used to reduce *TRE*. Many methods for reducing *TRE* fall into a category of Volumetric Error Compensation (VEC) techniques [16-19]. These modeling techniques require not only in-depth knowledge of robot and sensor but also knowledge on how to combine the residual errors from both systems into one error model. In addition, whenever a new perception system is integrated with a robot, a new analytical VEC model must be built while for the RRBC, the same general interpolation scheme can be reused. The RRBC method is easier to develop as it does not require formulation of complex, analytical error models. VEC techniques and RRBC method require the acquisition of comparable amounts of data to fit parameters for the theoretical model or to calculate the corrections, respectively.

Visual servo control is another common technique used to overcome problems created by localization error [20-22]. This technique comes in two main versions: Image-Based Visual Servoing (IBVS) and Position-Based Visual Servoing (PBVS). Each of the version has its own advantages and problems associated with convergence, stability and robustness. In visual servoing, the initial alignment of the robot and the object need not to be very accurate as the robot path is constantly corrected until the error between the desired and the actual point is below an acceptance threshold. Unlike the RRBC or VEC techniques or the method introduced in [12] which only modify the location of the final destination point, visual servoing is an iterative process which constantly modifies robot trajectory. Successful application of such iterative procedure was demonstrated by Xue et al. on industrial robot by reducing absolute error to less than 0.2 mm [23]. Other, non-visual servoing strategies have also been developed for assembly applications.

Another common approach to alleviate positional error is to use active compliance control based on feedback from force/torque (F/T) sensors. For example, Navarro-Gonzalez et al. used a neural network algorithm to process data from F/T sensors and to mitigate the effect of misalignment between the vision system and the robot's wrist [24]. Abdullah et al. investigated peg-in-hole operations and used data models constructed from F/T feedback to search for the hole center using a strategy that mimics human intuitive behavior [25]. Xu et al.

divided the contact zone around the hole into sixteen sectors and applied a k-dimensional (KD) Tree algorithm to partition the sectors efficiently, and to more accurately determine the location of the hole center [26].

While these strategies improve the assembly process, their performance is still degraded by the misalignment between sensor and robot frames. For example, a larger uncertainty of the starting point for the search of the hole center using F/T sensors led to increased search time [27]. Kaipa et al. generated singulation strategies for binned parts and showed that the probability of a successful singulation diminished with increasing error of the part position [28]. Mahler et al. reported that increased pose error of a part degraded the quality of grasp planning even after the application of sophisticated algorithms to reduce these errors [29]. Similar observations were reported by Liu and Carpin who showed that the convergence time for grasp planning was positively correlated while the probability of force closure was negatively correlated with increasing positional uncertainty [30]. Therefore, these active control techniques, as well as other, passive or hybrid compliance strategies [31-35], will still benefit from improved accuracy of the object's pose in the robot's frame.

3. REVIEW OF THE PROCEDURE

3.1. Rigid Body Registration

Rigid-body registration is a common procedure used to find the transformation (rotation $\boldsymbol{R}$ and translation $\boldsymbol{\tau}$) between two coordinate frames. It requires the measurement of $J \geq 3$ points $\{\boldsymbol{X}\}_J$ in one frame and the corresponding set of points $\{\boldsymbol{Y}\}_J$ in the second frame. If the rigid-body condition is satisfied, the distance between any two points, i, j, in one frame would be the same as determined in the other frame, i.e.

$$L_{i,j} = \|\boldsymbol{X}_i - \boldsymbol{X}_j\| - \|\boldsymbol{Y}_i - \boldsymbol{Y}_j\| \equiv 0. \quad (1)$$

Then, the transformation $\{\boldsymbol{R}, \boldsymbol{\tau}\}$ would map fiducials $\{\boldsymbol{X}\}_J$ exactly onto $\{\boldsymbol{Y}\}_J$ and the corresponding Fiducial Registration Error (*FRE*) would be zero. However, due to noise and possible bias in the measured fiducials, $L_{i,j} \neq 0$, and the best transformation (in the Least Squares sense) is computed by minimizing *FRE*

$$FRE(\boldsymbol{R}, \boldsymbol{\tau}) = \sqrt{\frac{1}{J}\sum_{j=1}^{J}\|\boldsymbol{R}\boldsymbol{X}_i + \boldsymbol{\tau} - \boldsymbol{Y}_j\|^2}. \quad (2)$$

Once the transformation is found, it can be used to transform target points $\{\boldsymbol{T}_X\}$ measured by a perception system to the robot frame. If target points $\{\boldsymbol{T}_Y\}$ are also measured in the robot frame (as is the case in this research study) then Target Registration Error (*TRE*) can be calculated

$$TRE(\boldsymbol{T}_X) = \|\boldsymbol{R}\,\boldsymbol{T}_X + \boldsymbol{\tau} - \boldsymbol{T}_Y\|. \quad (3)$$

While *FRE* is often used as a metric for registration quality, it has been shown that it can be very misleading and provide false assurance as to the quality of the registration [36, 37]. A much more reliable metric is based on a representative set of *N* targets distributed in the work volume and the Root Mean Square of *TRE* (RMS_T) for these targets:

$$RMS_T = \sqrt{\frac{1}{N}\sum_{n=1}^{N} TRE^2(n)}. \quad (4)$$

Calculation of RMS_T requires the measurement of targets $\{\boldsymbol{T}_Y\}$ in the second frame. Unlike fiducials, which must also be measured in both frames, targets are not used for determining the registration transformation.

3.2. Restoration of the Rigid Body Condition (RRBC)

The degree of deviation from the rigid body condition can be quantified by calculating the standard deviation, σ_L, of the differences $L_{i,j}$ in Eq. (1) over all possible pairs of fiducials. For *J* fiducials, there are $J(J-1)/2$ unique pairs. The purpose of RRBC is to reduce σ_L and, consequently, *FRE* exactly to zero. This is achieved by calculating *J* corrections $\{\boldsymbol{\varepsilon}\}_J$ in the vision sensor frame, and replacing the measured fiducials $\{\boldsymbol{X}\}_J$ with the corrected locations $\{\widehat{\boldsymbol{X}}\}_J$

$$\widehat{\boldsymbol{X}}_j = \boldsymbol{X}_j + \boldsymbol{\varepsilon}_j, \quad (5)$$

for $j = 1, \ldots, J$. The corrections $\{\boldsymbol{\varepsilon}\}_J$ are calculated using the inverse transformation in Eq. (2), i.e. by registering $\{\boldsymbol{Y}\}_J$ to $\{\boldsymbol{X}\}_J$

$$\boldsymbol{\varepsilon}_j = \boldsymbol{R}_{inv}\, \boldsymbol{Y}_j + \boldsymbol{\tau}_{inv} - \boldsymbol{X}_j \tag{6}$$

where the inverse transformation consists of $\boldsymbol{R}_{inv} = \boldsymbol{R}'$ (where $\boldsymbol{R}'$ is the transposed matrix) and $\boldsymbol{\tau}_{inv} = -\boldsymbol{R}_{inv}\, \boldsymbol{\tau}$. Once corrections to the fiducials $\{\boldsymbol{\varepsilon}\}_J$ are calculated, the correction to the n^{th} target, $\boldsymbol{T}_X(n)$, in the vision frame can be approximated using the corrections of the nearest fiducials. In this study, the target corrections are based on linear interpolation of the corrections from eight fiducials (corners of a cube centered at the target)

$$\boldsymbol{\varepsilon}(\boldsymbol{T}_X) = \textstyle\sum_{n=1}^{8} w_n \boldsymbol{\varepsilon}_n\,, \tag{7}$$

where w_n is the weight for the correction from the n^{th} fiducial and $\sum w_n = 1$. The corrected target position in vision frame is then

$$\widehat{\boldsymbol{T}}_X = \boldsymbol{T}_X + \boldsymbol{\varepsilon}(\boldsymbol{T}_X)\,. \tag{8}$$

When $\widehat{\boldsymbol{T}}_X$ is transformed to the robot frame, it is expected to result in a smaller $TRE(\widehat{\boldsymbol{T}}_X)$ in Eq. (3) than the corresponding error for an uncorrected target $TRE(\boldsymbol{T}_X)$.

As with any interpolation scheme, the accuracy of the correction in Eq. (7) depends on the distances between the target and its nearest fiducials. If the correction $\boldsymbol{\varepsilon}(\boldsymbol{X})$ is a continuous function at fiducial locations $\boldsymbol{X}$, then more accurate interpolated values are expected for decreasing distances between target and fiducials. By virtue of the same argument, more accurate correction $\boldsymbol{\varepsilon}(\boldsymbol{T}_X)$ is expected when nearby fiducials $\boldsymbol{X}_n$ and their corresponding corrections $\boldsymbol{\varepsilon}_n$ in Eq. (6) are obtained with arm configurations close to the target arm configuration. The next section describes the experimental set up, which was designed to test this hypothesis.

4. EXPERIMENTS

Two different robots operating in position control mode were used in the experiment: a Universal Robot UR5 which is a 6 degree-of-freedom (6DOF), collaborative robot arm and a KUKA LWR 4+ which is a 7DOF robot arm. The stiffness of both robots was set to high to ensure high accuracy in Cartesian space. According to the robot specification, the repeatability of the robot, σ_{rep}, was 0.1 mm for the UR5 and 0.05 mm for the KUKA.

A Spherical Infrared Reflector (SIR) was attached to the end of the robot arm and was tracked by an OptiTrack TRIO, which is a fixed three-camera motion capture system. Each of the three cameras has a resolution of 640 × 480 pixels, and the sampling frequency of the system was set to 120 Hz. The center of the $250 \times 300 \times 200$ mm UR5 work volume was 2.1 m away from the TRIO. For the KUKA, the center of the $240 \times 200 \times 200$ mm work volume was 1.8 m away from the TRIO.

In the experiment, the UR5 was operated using its controller and inverse kinematic module. For each commanded pose in Cartesian space, the module provided only one solution, and the end user did not have control over which of the multiple joint configurations was selected. For the KUKA, we implemented a custom Analytical Inverse Kinematic (AIK) module which yielded up to eight joint configurations corresponding to the same nominal pose in Cartesian space [38].

4.1. Data Acquisition with the UR5

The robot arm was commanded to move the SIR to a series of predefined positions in Cartesian space. The motion tracking system collected $K = 12$ repeat measurements at each position. The nominal SIR location in the robot frame was recorded, and the arm was then moved to the next nominal position. Three datasets were acquired: two with evenly distributed points throughout the whole work volume, and one with non-uniformly distributed points. In the first category, A, one dataset (A1) had $11 \times 13 \times 9$ points on a regular cubic grid, with the cube edge size $a = 25$ mm. The second dataset (A2) had $21 \times 25 \times 17$ points with $a = 12.5$ mm. After data collection, each dataset was divided into distinct target and fiducial subsets. For the A1 dataset, there were $5 \times 6 \times 4 = 120$ targets on a regular cubic grid with $a = 2 \times 25$ mm and 1,167 fiducials. For the A2 dataset, there were $10 \times 12 \times 8 = 960$ targets on a grid with $a = 2 \times 12.5$ mm and 7,965 fiducials. Fiducial points were used to calculate both the registration transformation and corrections $\{\boldsymbol{\varepsilon}\}_J$ in Eq. (6).

Datasets A1 and A2 were acquired to study the effect of distance between a target and its nearest fiducials on RMS_T. The acquisition of another dataset with points uniformly distributed throughout the entire work volume with an even smaller cube size a was not feasible due to the exponentially increasing amount of data and acquisition time. Therefore, a third dataset, B, was collected with non-uniformly distributed points. For this dataset, the same 120 target locations as in A1 were selected, but each target was surrounded by 80 fiducials, as shown in Figure 1. The fiducials were distributed into ten subgroups of eight fiducials. Each octuplet had fiducials located at the eight corners of a cube centered at the target location. The ten cubes had edge length a decreasing from 50 mm to 5 mm; corresponding target-fiducial distances are $d = \sqrt{3}a/2$, so $d_{max} = 43.3$ mm and $d_{min} = 4.33$ mm. The total number of points measured for this pattern is 120 × 81 = 9,720. At each point (target or fiducial), the motion tracking

system collected K = 12 repeat measurements of the SIR position. The output file for the UR5 contained the (x, y, z) commanded positions from the robot controller in robot frame, and the output file from the TRIO contained the corresponding (x, y, z) of SIR in TRIO frame.

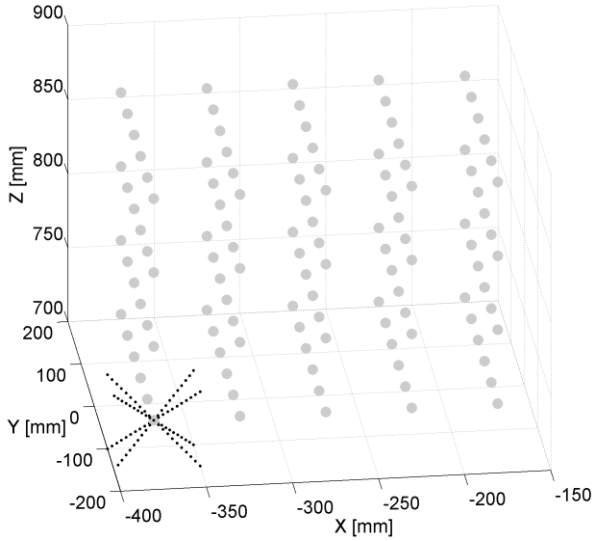

Figure 1. Locations of targets (large, grey dots) and 80 fiducials surrounding one target for dataset B. The same pattern of fiducials is repeated around each target, but for clarity, fiducials surrounding the other targets are not displayed.

4.2. Data Acquisition with the Kuka LWR 4+

The SIR was mounted at the end of the KUKA arm using a precision-machine standoff by Hexagon Metrology and a custom mounting plate manufactured by Misumi USA. The use of this high-accuracy mount provided the offsets from the end of the arm to the center of the SIR, circumventing the need to perform hand-eye calibration. The robot was commanded to move to $13 \times 11 \times 11$ points on a regular cubic grid, with the cube edge size $a = 20$ mm. Similar to the data acquired by UR5, each target was surrounded by eight fiducials which were the vertices of a cube centered at a target nominal location. The robot was commanded to go to nominal points on the grid in an organized, planned manner to minimize the total path length and to reduce acquisition time (two consecutive visited locations were always separated by length a, as shown in Figure 2).

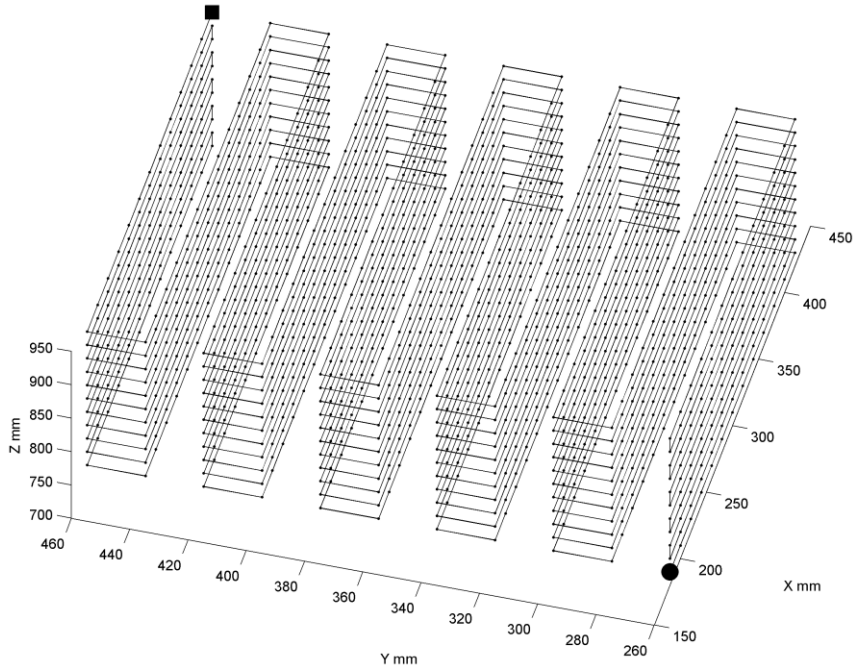

Figure 2. The pattern in which consecutive nominal points were visited by the KUKA. The large dot and square indicate the start and end points, respectively.

At each of the 1,573 nominal locations in Cartesian space, the AIK module calculated all configurations of joint angles. In the work volume used for this experiment, there were four arm configurations for each point in Cartesian space, see Figure 3. At each arm configuration, the TRIO recorded one measurement of the SIR location, so for each nominal location in Cartesian space, there were four slightly different locations of SIR. The same commanded point yielded four different locations of the tool tip due to the robot being out of calibration and other, hard to model effects such as thermal expansion, bending of the robot arm under its weight, or slack/slop in joints over time. The AIK provided four arm configurations in an arbitrary order. For each recorded location, the output file contained: 1) (x, y, z) of the commanded point in Cartesian space in robot frame; 2) seven joint angles $(\gamma_1, \ldots, \gamma_7)$ from the robot controller which described the configuration of 7DOF arm; 3) (x, y, z) of SIR location in sensor frame.

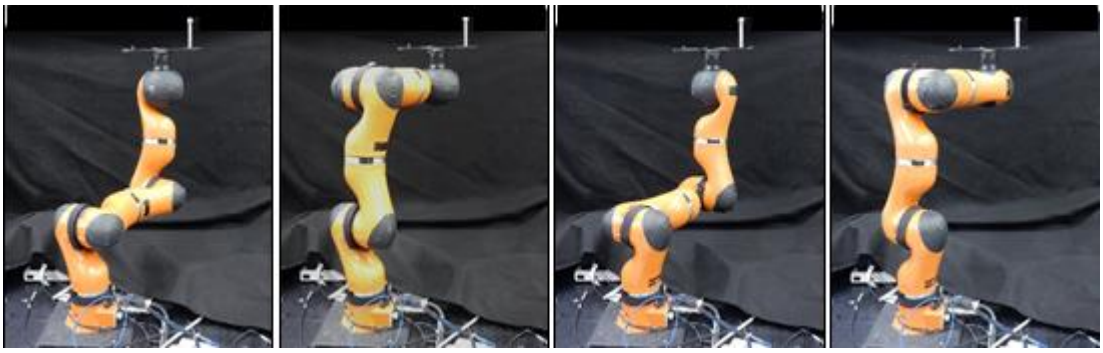

Figure 3. Four configurations of the KUKA arm corresponding to the same SIR location in Cartesian space.

4.3. Processing UR5 Data

Datasets in category A were used to estimate the average noise level of the vision system throughout the work volume. At each location, the variance from the 12 repeat measurements was determined. Then, the average variance over all locations was evaluated yielding the corresponding average standard deviation σ_{opt}. The combined average noise characteristics of the robot-camera system, denoted by σ_{noise}, was estimated as

$$\sigma_{noise} = \sqrt{\sigma_{opt}^2 + \sigma_{rep}^2} \tag{9}$$

To characterize the deviation from the rigid-body condition, the differences L defined in (1) were calculated using averaged positions $\{\overline{\boldsymbol{X}}\}_J$ in the perception system frame. The histograms of the differences for datasets A1 and A2 were similar, and the histogram for dataset A2 is shown in Figure 4; the corresponding standard deviations σ_L were also determined. For each dataset, A1 and A2, all fiducials were used to determine the registration transform $\{\boldsymbol{R}, \boldsymbol{\tau}\}$ between the perception system and the robot frame. From this, corrections $\{\boldsymbol{\varepsilon}\}_J$ were then evaluated and, finally, $corRMS_T$ and $uncRMS_T$ were calculated with Eq. (4) using the corrected $TRE(\widehat{\boldsymbol{T}}_X)$ and uncorrected $TRE(\boldsymbol{T}_X)$, respectively.

For dataset B, the average location from the 12 repeat measurements acquired with the perception system was calculated at each location. The robot frame was then registered to the perception system frame using all J = 9,600 fiducials to determine $\{\boldsymbol{R}, \boldsymbol{\tau}\}$. The interpolated corrections for each of the 120 targets were calculated 10 times using Eq. (7), once for each octuplet of surrounding fiducials located at the corners of the 10 cubes of diminishing size. Since the target was located in the center of each of the 10 cubes, all weights w_n in Eq. (7) were equal and set to 1/8. For each cube size d, the corresponding corrected n^{th} target, $\widehat{\boldsymbol{T}}_X(n, d)$, was transformed to the robot frame using $\{\boldsymbol{R}, \boldsymbol{\tau}\}$, and the corrected target error $TRE(\widehat{\boldsymbol{T}}_X(n), d)$ was calculated for each target. Then, the corrected $corRMS_T(d)$ was evaluated for each distance d using the corrected individual $TRE(\widehat{\boldsymbol{T}}_X(n), d)$.

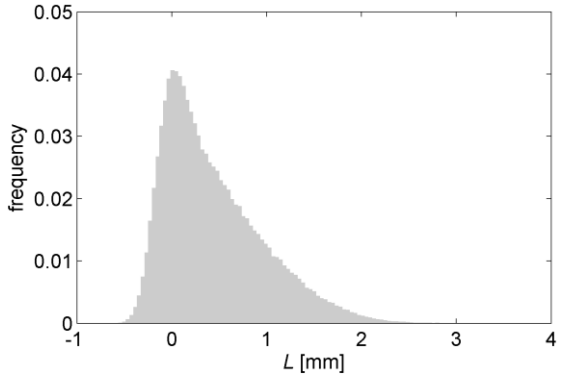

Figure 4. Histogram of occurrences of differences L for dataset A2.

4.4. Processing Kuka LWR 4+ Data

The acquired collection of points was divided into distinct target and fiducial subsets: there were $6 \times 5 \times 5$ nominal target locations distributed on a regular cubic grid with size $d =$

2×20 mm. All remaining nominal locations served as fiducials. Thus, there were 150 targets and 1,423 fiducials where each target location was at the center of a cube of size d defined by eight fiducials. At each nominal location (target or fiducial) there were four measurements from the TRIO corresponding to four different arm configurations. The data were processed four times, independently for each recorded arm configuration. The correction to each target was interpolated from the eight nearest fiducials using three processing strategies.

In Strategy 1, the data were processed in the order as dictated by the order of the four configurations provided by the AIK module. In Strategy 2, the data was reorganized and ordered in the following way. The first joint configuration for the first nominal commanded point (large dot in Figure 2) was set as the reference configuration. The remaining three configurations were sorted in ascending order according to the distance (in 7DOF space) to the reference configuration. During the sorting process, if any two configurations had to be switched, all data associated with that measurement were also switched. Then, for the second nominal point, the configuration closest to the reference configuration from the first nominal point was found and became the new reference configuration, and the remaining three configurations were ordered in the same way as for the first nominal point. The process continued in a sequential way with the first configuration of the previous point serving as the reference configuration of the next point until the last nominal point (large square in Figure 2) was reached. The purpose of such data shuffling was to minimize the number of instances where sequential locations have m-th ($m = 1, \ldots, 4$) point measured by the TRIO in two very different arm configurations.

Histograms of the differences L defined in Eq. (1) were built for all four configurations, and both processing strategies, unordered and ordered, are shown in Figure 5 and Figure 6, respectively. Note that the configurations as labeled in Figure 5 and Figure 6 are not necessarily the same, as explained above. The values of corresponding standard deviations σ_L were also calculated.

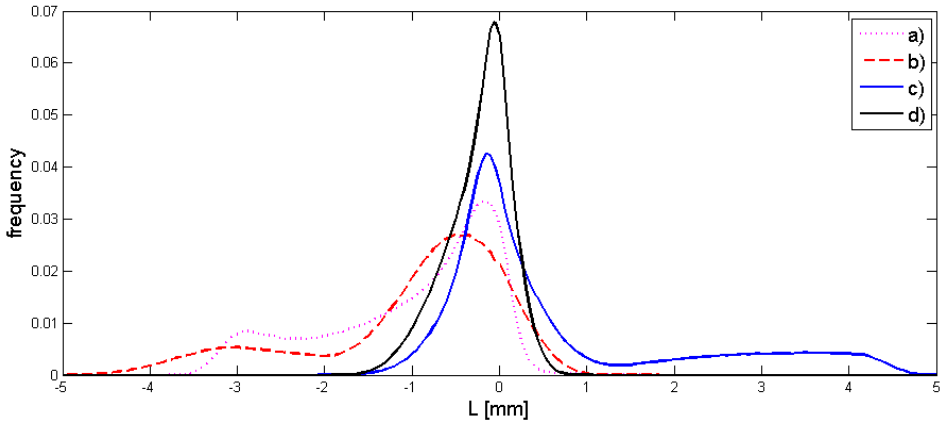

Figure 5. Histograms of the differences L calculated for each of the four configurations (a – d) for unordered data (Strategy 1).

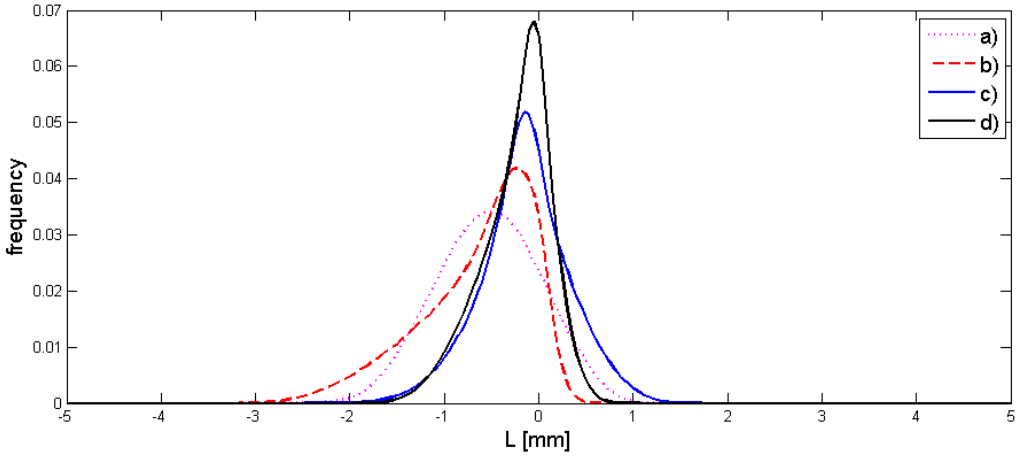

Figure 6. Histograms of the differences L calculated for each of the four configurations (a – d) for ordered data (Strategy 2).

In Strategies 1 and 2, a separate registration transformation $\{\boldsymbol{R}, \boldsymbol{\tau}\}$ was calculated using all fiducials for each of the four configurations. Then, for each transformation, the corresponding corrections $\boldsymbol{\varepsilon}_j$ to fiducial locations in sensor frame were calculated using Eq. (7). For the unordered strategy, Strategy 1, corrections to each target were calculated and the uncorrected $TRE(\boldsymbol{T}_{X,m})$ as well the corrected $TRE(\widehat{\boldsymbol{T}}_{X,m})$ were calculated for each m-th configuration. From all $n = 1, \ldots, 150$ individual $TRE(n, m)$, the resulting $uncorRMS_T(m)$ and $corRMS_T(m)$ were calculated for each configuration. The same calculations were repeated for the ordered strategy, Strategy 2.

In practical applications, very accurate target positions in the work volume may only be needed in a few locations and each location may be measured in a different arm configuration. Strategy 2 requires that all targets and fiducials be measured in one similar configuration and a separate registration is needed for each different configuration; this is very restrictive and not very practical. Therefore, we processed the data using a third strategy to better simulate field conditions. For each target, the correction was interpolated from eight surrounding fiducials (corners of a cube centered at target) in such way that each selected fiducial had an arm configuration closest (in 7DOF space of joint angles) to the target configuration. For Strategy 3, only one registration transformation $\{\boldsymbol{R}, \boldsymbol{\tau}\}$ was calculated and used to process all four configurations. The registration was based on the eight fiducials (each with an arm configuration randomly selected from the four measured configurations) at the corners of the entire work volume shown in Figure 2.

5. RESULTS

5.1. Effect of Distance Between Target and Fiducial

A summary of the results obtained from datasets A1 and A2 acquired with the UR5 is provided in Table 1. For both datasets, the parameter $\rho = \sigma_L/\sigma_{noise}$ was greater than 2.5, i.e., deviation from the rigid-body condition is caused mainly by systematic factors. Experiments reported in [39] indicated that for these situations, the RRBC method can be applied and can lead to reduced target errors. On average, the errors for the corrected targets are smaller than for the uncorrected targets, as is evident from the ratio $\gamma = (uncRMS_T - corRMS_T)/uncRMS_T$. It is expected that the registration error would decrease as the distance *d* between the target and its nearest fiducials decreased, and this is confirmed by comparing $corRMS_T$ for A2 with that for A1. This finding was systematically checked using dataset B where $corRMS_T$ was calculated for ten different distances and the same set of targets, see Figure 7. The $uncRMS_T$ for dataset B acquired with UR5 was 0.650 mm, close to the corresponding value for A1. Thus, for the smallest distance d_{min}, RMS_T was reduced by $\gamma = 84\%$.

Table 1. Summary of results from data in category A acquired with UR5

Data	d [mm]	σ_{opt} [mm]	σ_L [mm]	σ_{noise} [mm]	ρ	$uncRMS_T$ [mm]	$corRMS_T$ [mm]	γ [%]
A1	43.3	0.058	0.626	0.114	5.5	0.666	0.240	64
A2	21.6	0.059	0.522	0.116	4.5	0.603	0.168	72

The RMS_T calculated in Eq. (4) for the uncorrected or corrected targets is the average of all individual errors $TRE(n), n = 1, \ldots, N$. Since the correction $\boldsymbol{\varepsilon}(\boldsymbol{T}_X(n))$ to n^{th} target is estimated by linear interpolation from the eight neighboring fiducials using Eq. (7), in some N_{bad} target locations the RRBC method may fail, and the corrected target error may be larger than the uncorrected error, i.e., $TRE(\hat{\boldsymbol{T}}_X) > TRE(\boldsymbol{T}_X)$. While decreasing $corRMS_T(d)$ by decreasing the distance *d* is beneficial, it is equally important to verify that the number of bad locations $N_{bad}(d)$ is small and decreases with *d*. Figure 8 shows that this is indeed the case; out of a total $N = 120$ targets locations, the application of the RRBC method led to only $N_{bad}(d_{min}) = 4$ failures for the smallest measured distance *d* compared to $N_{bad}(d_{max}) = 17$.

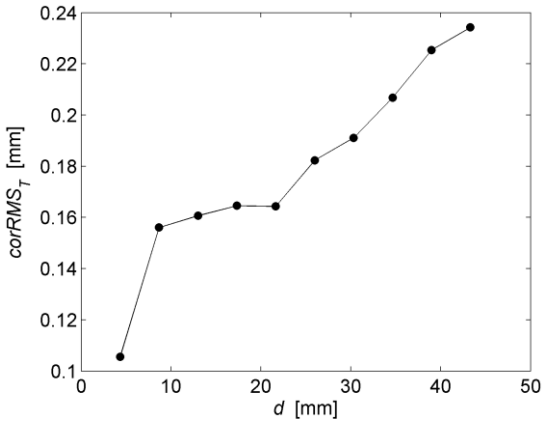

Figure 7. Dependence of corrected target error corRMS_T vs. distance d for dataset B.

More detailed information about the errors at locations where the RRBC method failed is provided in Figure 9 where the errors for the largest d_{max} and the smallest d_{min} distances are shown. Closer inspection of the results, displayed in Figure 9b, shows that for target n = 2 and n = 17, the difference between corrected target error $TRE(\hat{\boldsymbol{T}}_X)$ (grey bar) and uncorrected $TRE(\boldsymbol{T}_X)$ (black bar) is marginal. Thus, for the smallest distance, failure of the RRBC method and substantial relative increase of TRE was observed only in 2 out of 120 target locations.

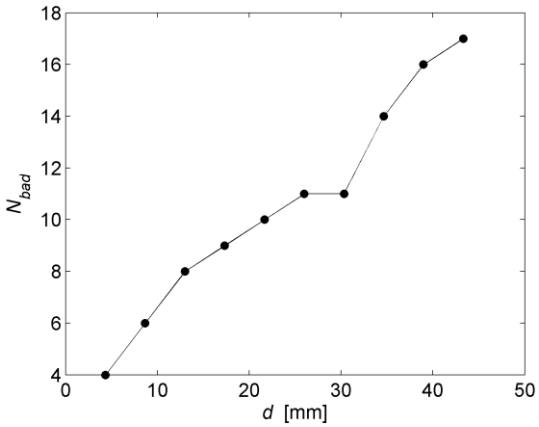

Figure 8. The total number of bad target locations N_{bad} where RRBC failed (corrected target error larger than uncorrected error) vs. distance d. Total number of targets in dataset B is N = 120.

In Figure 10, the 3D locations where the RRBC failed for the largest distance d_{max} (marked by dark grey dots) and for the smallest distance d_{min} (marked by black dots) are plotted. It is worth noting that three out of four points where RRBC failed for d_{min} are located on the lowest layer of targets, corresponding to the smallest z coordinate. The fourth failed location is on the top layer of targets with the largest z. Targets labeled n = 1 and n = 5 in Figure 9b are in the local region characterized by strong nonlinearity where linear interpolation yields poor estimates of the target correction – in spite of $d = d_{min}$.

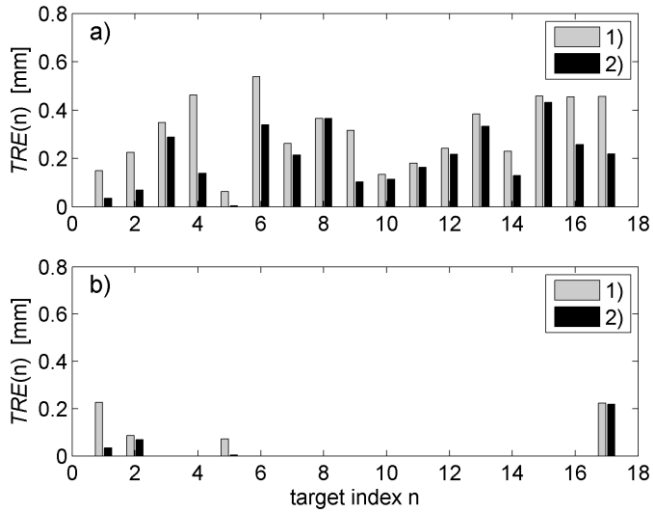

Figure 9. *TRE* at target locations where RRBC failed for dataset B: a) for the largest distance d_{max}; b) for d_{min}. Grey bars 1) indicate corrected target errors $TRE(\hat{\mathbf{T}}_X)$ and black bars 2) are uncorrected errors $TRE(\mathbf{T}_X)$.

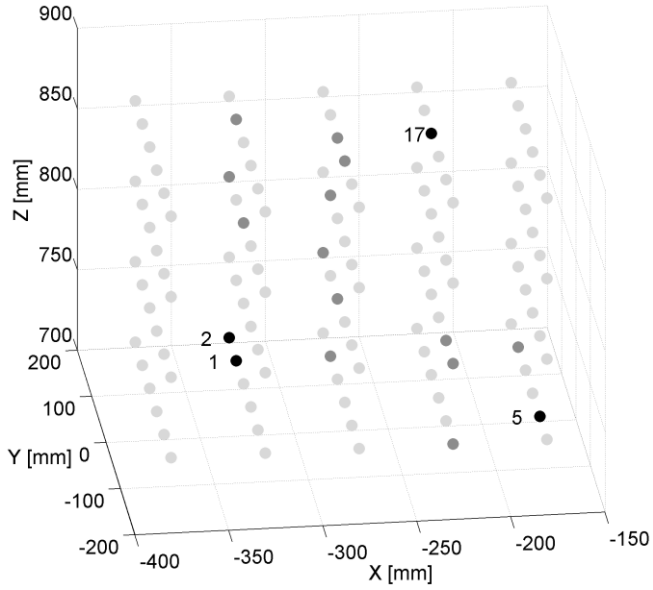

Figure 10. Location of targets for dataset B. Light grey dots are where RRBC was successful for all ten values of *d*. Dark grey dots are locations where RRBC failed for d_{max}. Black dots are where RRBC failed for both d_{max} and d_{min}. Numbers next to black dots correspond to the target index *n* in Figure 9b.

However, for a majority of target locations, linear interpolation worked well. To show the improvement in individual target errors, a histogram of differences ΔTRE is shown in Figure 11 where $\Delta TRE = TRE(\hat{\boldsymbol{T}}_X) - TRE(\boldsymbol{T}_X)$ is the difference between the corrected and uncorrected target error at locations where RRBC succeeded (i.e., $\Delta TRE < 0$).

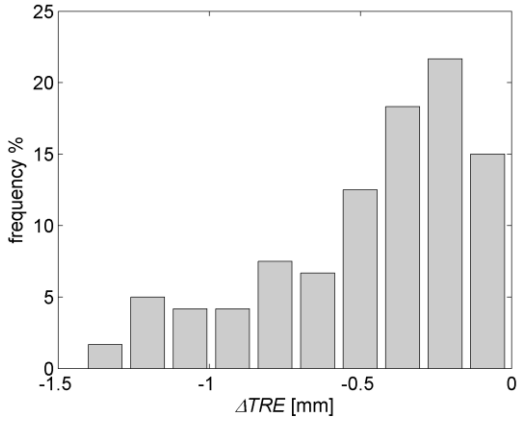

Figure 11. Histogram of the differences of target errors ΔTRE where RRBC succeeded for smallest distance, d_{min}, between target and nearby fiducials.

5.2. Effect of Arm Configuration

A summary of results obtained from the data acquired with the KUKA is provided in Table 2. Standard deviations σ_L for each *m*-th configuration and both unordered and ordered strategies (1 and 2, respectively) were calculated for differences L: their corresponding histograms are displayed in Figure 5 and Figure 6. Parameter $\rho = \sigma_L/\sigma_{noise}$ was calculated using Eq. (9) with σ_{opt} equal to that for dataset A1 in Table 1 and manufacturer specified σ_{rep} which yielded $\sigma_{noise} = 0.077$ mm. Roughly 14 % of nominal locations were switched in the process to order data. All switches occurred in configurations 1-3: no switch was needed for configuration 4. Therefore, all results for the fourth configuration for Strategies 1 and 2 in Table 2 are the same.

Table 2. Summary of results obtained from data acquired with KUKA

m-th config	σ_L [mm]		ρ		$uncRMS_T$ [mm]			$corRMS_T$ [mm]			γ [%]		
Strategy	1	2	1	2	1	2	3	1	2	3	1	2	3
1	0.977	0.558	12.8	7.3	1.166	0.637	2.956	0.391	0.149	0.173	66	77	94
2	1.120	0.604	14.6	7.9	1.242	0.716	1.793	0.431	0.177	0.151	65	75	92
3	1.425	0.476	18.6	6.2	1.516	0.489	2.430	0.659	0.151	0.155	57	69	94
4	0.373	0.373	4.9	4.9	0.398	0.398	2.436	0.146	0.146	0.146	63	63	94

Target Registration Errors for all $N = 150$ targets measured in $m = 1$ arm configuration and for Strategy 1 (unordered data) are shown in Figure 12. Similar results were obtained for configurations $m = 2, 3$. No large spikes in TRE, as seen in Figure 12, were observed for $m = 4$ configuration. The errors calculated for Strategy 2 (ordered data, $m = 1$) are shown in Figure 13. The remaining three configurations $m = 2, 3, 4$ yielded similar results. The resulting RMS_T for all four configurations in Strategies 1 and 2 are shown in Figure 14 and Figure 15, respectively.

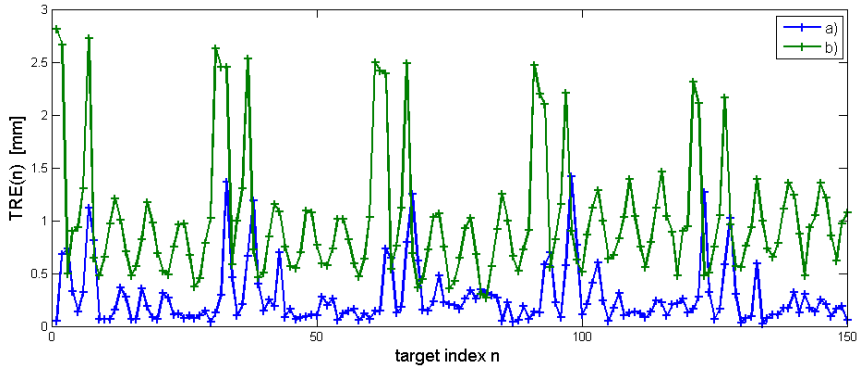

Figure 12. Target Registration Error for Strategy 1 (unordered): a) for corrected by RRBC errors $TRE(\hat{\mathbf{T}}_{X,n})$; b) for uncorrected errors $TRE(\mathbf{T}_{X,n})$. SIR position measured in $m = 1$ robot arm configuration.

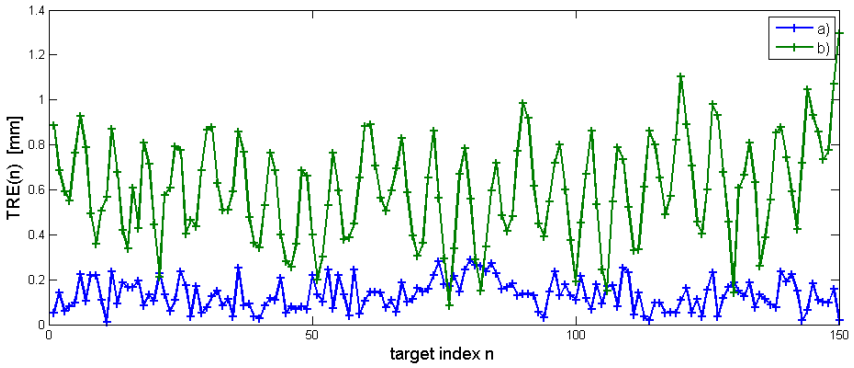

Figure 13. Target Registration Error for Strategy 2 (ordered): a) for corrected by RRBC errors $TRE(\hat{\mathbf{T}}_{X,n})$; b) for uncorrected errors $TRE(\mathbf{T}_{X,n})$. SIR position measured in $m = 1$ robot arm configuration.

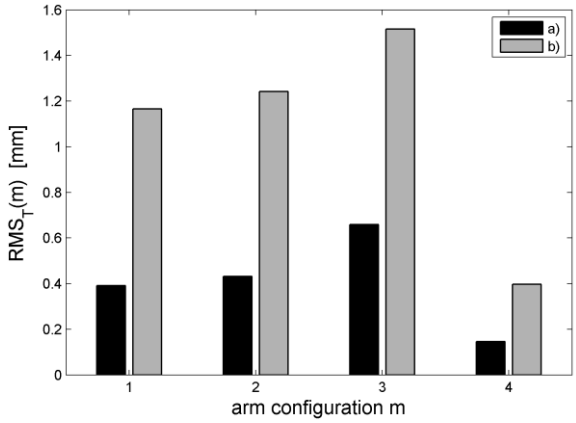

Figure 14. RMS_T for Strategy 1 (unordered): a) for corrected by RRBC errors corRMS_T; b) for uncorrected errors uncRMS_T.

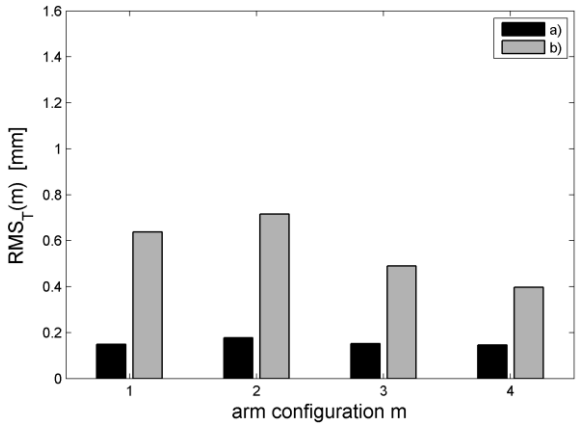

Figure 15. RMS_T for Strategy 2 (ordered): a) for corrected by RRBC errors corRMS_T; b) for uncorrected errors uncRMS_T.

6. DISCUSSION

Two procedures to improve the performance of the RRBC method were investigated. The presented results for the first procedure confirm that, by decreasing the distance d between target $\boldsymbol{T}_X$ and nearby fiducials, a more accurate estimate of the correction to target location $\boldsymbol{\varepsilon}(\boldsymbol{T}_X)$ can be achieved. This, in turn, leads to smaller target registration error. The monotonic decrease of $corRMS_T$ for decreasing d shown in Figure 7 indicates that linear interpolation of non-linear correction function $\boldsymbol{\varepsilon}$ is sufficient and higher order interpolation schemes are not necessary. Clustering of failed locations on the boundary of the work volume displayed in Figure 10 is the consequence of stronger local nonlinearity in these locations. Determining the upper limit of d for which linear interpolation is sufficient depends on the characteristics of the particular vision-robot system and must be determined on a case by case basis. However, there is also a lower limit for d and possible reduction in RMS_T since the RRBC method was shown to be beneficial only if the parameter $\rho > 2.5$ [39]. Since the noise characteristic, σ_{noise}, can be consider a constant, the smallest possible distance d_{min} between the target and any nearby fiducials must satisfy the criterion

$$d_{min} > 2.5\,\sigma_{noise} \tag{9}$$

As mentioned earlier, to ensure that the distance between nearby fiducials and an arbitrarily located target somewhere in the work volume is small, a large number of fiducials must be measured throughout the volume. Depending on the size of the volume and the desired spacing between measured fiducials, the amount of collected data may grow significantly, limiting the practicality of the proposed procedure. However, assembly operations may not always require accurate positioning of the end effector throughout the entire robot work volume. Limiting where accurate positioning is required will dramatically reduce the amount of data that needs to be collected.

If a part's pose is determined by a vision system by measuring a few M points (either external targets attached to the part, or points which are detected by the system trained earlier to recognize characteristic features of the part) then only these M points need to be known with high accuracy. It is reasonable to assume that during automated assembly, the part is placed in approximately the same location in the work volume for each operation cycle. If the variation of the part's placement (i.e., the position uncertainty) is $\pm s$, then it is sufficient to capture a dense collection of fiducial measurements on a regular grid in M cubes, each of size $2s$. This procedure is schematically illustrated in Figure 16, where the coordinate frames of the robot and vision system are fixed in the World frame. The estimated correction at the target location could be obtained using linear interpolation Eq. (7). However, since the target may be in an arbitrary location relative to the nearby fiducials, weights w_n in Eq. (7) will not be equal and should be evaluated dynamically using, for example, a common trilinear interpolation scheme [40].

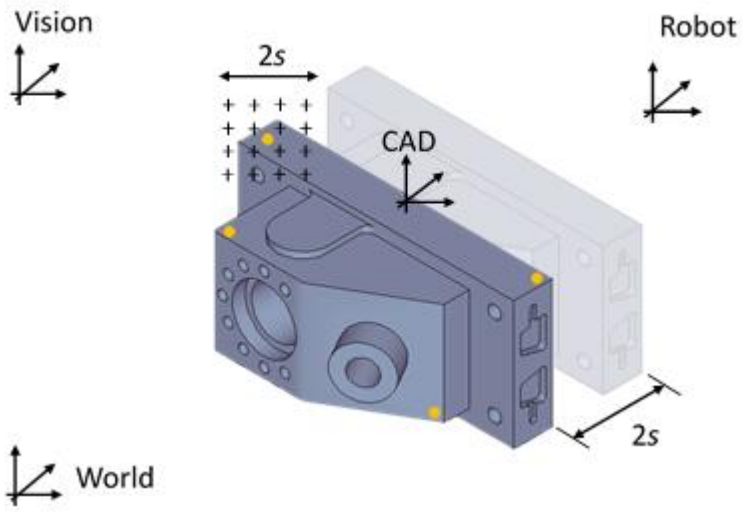

Figure 16. Schematic of a procedure for identifying fiducial locations to improve vision-robot registration. *M* = 4 targets (orange dots) are used to determine the pose of the object in vision frame. For clarity, fiducial locations (marked by crosses) surrounding only one target are shown

In the second procedure, the performance of the RRBC method was improved by selecting fiducials measured in arm configurations closest to the configuration in which target position was acquired. By avoiding the use of points in the work volume measured in substantially different arm configurations, the rigid body condition can be better preserved as confirmed by comparing the standard deviations σ_L for Strategies 1 and 2 in Table II and the corresponding histograms of differences L in Figure 5 and Figure 6. The use of similar arm configurations led to larger reductions of the target registration errors - compare plots of TRE for Strategy 2 in Figure 13 with Strategy 1 in Figure 12. Errors for the uncorrected targets $TRE(\boldsymbol{T}_{X,n})$ in Figure 12b are less than 1.5 mm for all but a few targets where the errors spike to almost 2.5 mm. The targets with large errors correspond to the locations where the target arm configurations were different from the arm configurations for the fiducials; recall that for the unordered strategy, the registration transformation $\{\boldsymbol{R}, \boldsymbol{\tau}\}$ was calculated from all fiducials for each of the four configurations. This leads to locally discontinuous registration error at these target locations. Target corrections using the RRBC method reduced the TRE substantially for the most of the target locations, but for some targets, the method was less effective due to the application of linear interpolation to locally discontinuous error function, as can be seen in Figure 12a. No spikes in *TRE* were observed for the ordered strategy for both uncorrected $\boldsymbol{T}_{X,n}$ and corrected $\widehat{\boldsymbol{T}}_{X,n}$ target locations, as shown in Figure 13. The RBBC method reduced the target errors for both unorder and ordered data (Strategies 1 and 2). However, Strategy 2 yielded larger reductions and smaller errors of the corrected targets than Strategy 1, as evidenced by the plots of $uncRMS_T$ and $corRMS_T$ in Figure 14 and Figure 15.

Of the three strategies, the Strategy 3 yielded the largest error reduction γ - greater than 90% (see Table II). However, this high reduction is deceptive as it is caused by unusually large errors for the uncorrected target (compare the $uncRMS_T$ for Strategies 2 and 3 in Table II) and comparable $corRMS_T$ for both Strategies 2 and 3. Recall that for Strategy 3, only one

registration transformation $\{\boldsymbol{R}, \boldsymbol{\tau}\}$ based on eight fiducials was calculated to process the data acquired for all four arm configurations and could be the cause of the unusually large uncorrected errors. The results obtained for Strategy 3 show that even if the registration is poor, small target registration error is achievable if the target location is corrected by the RRBC method. A similar conclusion was drawn in [23] where inaccurate registration was compensated by a series of corrections leading to an acceptable level of the final error. The main difference between the enhanced RRBC method and the iterative method used in [23] is that RRBC modifies only one, final commanded point. This feature may be more advantageous in some assembly applications than the use of an iterative scheme to control robot position. It should be noted that using a very large number (~ 1000) of fiducials in regular registration instead of using the RRBC method to reduce target error is not beneficial. The presented data for both robot arms clearly show that high reduction rates of RMS_T are still possible for all three datasets (A1, A2, B for UR5) and both processing Strategy 1 and 2 for KUKA even when all fiducials were used for registration.

We note that the $corRMS_T$ for Strategies 2 and 3 have almost the same value, independent of arm configuration. This is in contrast to Strategy 1 where the $corRMS_T$ showed a dependency with arm configuration, as shown in Table II. Thus, not only do Strategy 2 and 3 lead to improved performance of the RRBC method as measured by the degree of reduction of target errors, but they also made the errors of targets measured in different arm configurations more uniform in magnitude. Large variations in the errors associated with different arm configurations are generally undesirable because in some situations, physical constraints may eliminate configurations with small errors leaving only configurations with large errors. Thus, both Strategy 2 and 3 offer more flexibility in task planning; however, Strategy 3 is more practical as it utilizes one registration (based on fiducials in arbitrary configurations) to targets in different configurations while Strategy 2 requires ordering of the data so that all targets and fiducials are measured in a similar arm configuration and different configurations require different registrations.

Both Strategies 2 and 3 and Zeng's *et al*. [12] error similarity method make use of the following observation: two close (in joint angles space) arm configurations will have similar positional errors in Cartesian space. There are two main differences between the RRBC and Zeng's *et al*. method: 1) we estimate correction to a target position by local, linear interpolation from nearby fiducials while the global model of error was built based on error similarity in the entire work volume; 2) our interpolation scheme does not differentiate between kinematic and non-kinematic errors while the error similarity approach models non-kinematic errors as Gaussian noise. While modeling non-kinematic errors caused by thermal expansion or bending of the robot arm under its weight is difficult, nevertheless the root cause of these errors is systematic in nature and modeling them as Gaussian noise may not always be correct. The values of $corRMS_T$ reported in this paper are comparable to the reduced errors reported in [12] and the final errors in [23], the differences may be caused by different robots used in these studies. Thus, all three methods, enhanced RRBC, error similarity method [12], and the iterative correction method in [23], can be used to substantially reduce TRE. The determination of which is more advantageous will depend on the particular application and existing conditions. As the authors in [21] concluded: "*As with most engineering questions, there is no definite answer – only a set of performance tradeoffs to consider.*"

It was shown in a related study that reduced RMS_T is correlated with a better outcome of peg insertion [41]. When RMS_T was reduced by 60 %, this level of improvement led to a 4- to 11-fold reduction in the failed insertion rate, depending on the peg-hole tolerances. The reported improvement in insertion rate was obtained for the same robot as used in the current study (UR5), and the robot was also operated in position control mode (i.e., no sensor-driven search algorithm, remote center of compliance, or active F/T feedback was applied). Due to the test bed hardware used in that study (specifically, an optical table), only in-plane (i.e., lateral 2D) corrections to hole locations were applied. Such an insertion is very challenging as its success depends almost entirely on the correct localization of objects in the robot frame. It is reasonable to expect that even better improvement in peg-in-hole operation can be achieved when the procedures outlined in this study are applied, provided that the locations of targets in CAD frame are correct.

7. CONCLUSIONS

Robots are characterized by their good repeatability. At the same time, due to imperfect calibration during the remastering process of the joint-offsets, drift, or other less-controllable material factors, the robot's accuracy may be more than an order of magnitude worse than the specified repeatability. When such robots are integrated with vision sensors characterized by low noise, the resulting autonomous system may underperform due to poor registration between the vision system and the robot. An existing method for improving robot registration is enhanced by two procedures that further reduce registration error, provide robustness to arm configurations, and can lead to improved performance of autonomous systems in manufacturing applications.

Since we showed that the accuracy of the correction to the target location increases with decreasing distance between a target and its fiducials, users can select larger or smaller distances based on the required accuracy for their specific application. Improvement in the performance of the RRBC was also observed when fiducials closest to the target (in Cartesian space) have joint configurations similar to the target arm configuration. The RRBC method can therefore compensate for discontinuities in the registration error by including knowledge of arm configuration. Thus, there will be no performance degradation if the arm needs to be in different configurations to accommodate physical constraints in its workspace.

References

[1] R. Usubamatov, S. A. Adam, and A. Harun, "Analyzing the jamming of parts on the shaft in assembly processes," *Assembly Automation*, vol. 32, no. 4, pp. 340-346, 2012.

[2] W.Zhu, B.Mei, G.Yan, and Y.Ke, "Measurement error analysis and accuracy enhancement of 2D vision system for robotic drilling," *Robotics and Computer-Integrated Manufacturing*, vol. 30, pp. 160-171, 2014.

[3] L.Tingelstad, A.Capellan, T.Thomessen, and T.K.Lien, "Multi-Robot Assembly of High-Performance Aerospace Components," presented at the 10th IFAC Symposium on Robot Control, Dubrovnik, Croatia, 2012.

[4] J. Ross, K. Harding, and E. Hogarth, "Challenges faced in applying 3D noncontact metrology to turbine engine blade inspection," in *Proc. SPIE Dimensional Optical Metrology and Inspection for Practical Applications*, San Diego, CA, 2011, vol. 8133, pp. 81330H-1 - 81330H-9.

[5] C. Liu, Y. Li, and X. Hao, "An adaptive machining approach based on in-process inspection of interim machining states for large-scaled and thin-walled complex parts," *Int. J. Advanced Manufacturing Technology*, vol. 90, pp. 3119-3128, 2017.

[6] J. Gao, N. Gindy, and X. Chen, "An automated GD&T inspection system based on non-contact 3D digitization," *Int. Journal of Production Research*, vol. 44, no. 1, pp. 117-134, 2006.

[7] F. Franceschini, M. Galetto, D. Maisano, and L. Mastrogiacomo, "Large-scale dimensional metrology (LSDM): from tapes and theodolites to multi-sensor systems," *Int. J. Precision Engineering and Manufacturing*, vol. 15, no. 8, pp. 1739 - 1758, 2014.

[8] C. Mineo, S. G. Pierce, P. I. Nicholson, and I. Cooper, "Robotic path planning for non-destructive testing – A custom MATLAB toolboxapproach," *Robotics and Computer-Integrated Manufacturing*, vol. 37, pp. 1-12, 2016.

[9] C. Mineo, S. G. Pierce, B. Wright, I. Cooper, and P. I. Nicholson, "PAUT inspection of complex-shaped composite materials through six DOFs robotic manipulators," *Insight - Non-Destructive Testing and Condition Monitoring*, vol. 57, no. 3, pp. 161-166, 2015.

[10] M. Shah, "Solving the Robot-World/Hand-Eye Calibration Problem using the Kronecker Product," *J. Mechanisms and Robotics,* vol. 5, no. 3, pp. 031007-031007-7, 2013.
[11] M.Franaszek and G.Cheok, "Method to Improve Point-Based Registration by Restoring Rigid-Body Condition," *National Institute of Standards and Technology Report NISTIR,* vol. 8180, 2017.
[12] Y. Zeng, W. Tian, D. Li, X. He, and W. Liao, "An error-similarity-based robot positional accuracy improvement method for a robotic drilling and riveting system," *Int. J. Advanced Manufacturing Technology,* vol. 88, pp. 2745 - 2755, 2017.
[13] M.Holden, "A review of geometric transformations for nonrigid body registration," *IEEE Trans. Medical Imaging,* vol. 27, no. 1, pp. 111-128, 2008.
[14] A.Sotiras, Ch.Davatzikos, and N.Paragios, "Deformable medical image registration: A survey," *IEEE Trans. on Medical Imaging,* vol. 32, no. 7, pp. 1153-1190, 2013.
[15] F. P. M. Oliveira and J. M. R. S. Tavares, "Medical image registration: a review," *Computer Methods in Biomechanics and Biomedical Engineering,* vol. 17, no. 2, pp. 73-93, 2014/01/25 2014.
[16] M. Galetto, L. Mastrogiacomo, G. Moroni, and S. Petrò, "Volumetric Error Compensation for the MScMS-II," in *12th CIRP Conference on Computer Aided Tolerancing,* 2013, pp. 98 - 104: Elsevier.
[17] C. Cajal, J. Santolaria, D. Samper, and J. Velazquez, "Efficient volumetric error compensation technique for additive manufacturing machines," *Rapid Prototyping Journal,* vol. 22, no. 1, pp. 2 - 19, 2016.
[18] D. A. Bristow, M. Tharayil, and A. G. Alleyne, "A Survey of Iterative Learning Control," *IEEE Control Systems Magazine,* vol. June pp. 96-114, 2006.
[19] B.Muralikrishnan *et al.*, "Volumetric performance evaluation of a laser scanner based on geometric error model " *Precision Engineering,* vol. 40, pp. 139-150, 2015.
[20] K..Fathian, J..Jin, S.-G. Wee, D.-H. Lee, Y.-G. Kim, and N. R. Gans, "Camera relative pose estimation for visual servoing using quaternions," *Robotics and Autonomous Systems,* vol. 107, pp. 45-62, 2018.
[21] F. Chaumette and S. Hutchinson, "Visual Servo Control Part I: Basic approaches," *IEEE Robotics and Automation Magazine,* vol. 13, no. 4, pp. 82-90, 2006.
[22] F. Chaumette and S. Hutchinson, "Visual Servo Control Part II: Advanced Approaches," *IEEE Robotics and Automation Magazine,* vol. 14, no. 1, pp. 109 - 118, 2007.
[23] B. Xue, J. Zhu, Z. Zhao, J. Wu, Z. Liu, and Q. Wang, "Validation and mathematical model of workspace Measuring and Positioning System as an integrated metrology system for improving industrial robot positioning," *Proc. of the Institution of Mechanical Engineers, PartB: J. Engineering Manufacture,* vol. 228, no. 3, pp. 422 - 440, 2014.
[24] J.L.Navarro-Gonzalez, I.Lopez-Juarez, K.Ordaz-Hernandez, and R.Rios-Cabrera, "On-line incremental learning for unknown conditions during assembly operations with industrial robots," *Evolving Systems,* vol. 6, no. 2, pp. 101-114, 2015.
[25] M.W.Abdullah, H.Roth, M.Weyrich, and J.Wahrburg, "An Approach for Peg-in-Hole Assembling using Intuitive Search Algorithm based on Human Behavior and Carried by Sensors Guided Industrial Robot," *IFAC-PapersOnLine,* vol. 48, no. 3, pp. 1476-1481, 2015.
[26] Y.Xu, Y.Hu, and L.Hu, "Precision Peg-in-Hole Assembly Strategy Using Force-Guided Robot," presented at the 3rd Int. Conf. on Machinery, Materials and Information Technology Applications (ICMMITA), Qingdao, China, 2015.
[27] K. V. Wyk, M.Culleton, J.Falco, and K.Kelly, "Comparative Peg-in-Hole Testing of a Force-based Manipulation Controlled Robotic Hand," *IEEE Trans. on Robotics,* 2018.
[28] K. N. Kaipa *et al.*, "Addressing perception uncertainty induced failure modes in robotic bin-picking," *Robotics and Computer-Integrated Manufacturing,* vol. 42, pp. 17-38, 2016.
[29] J.Mahler *et al.*, "Dex-Net 1.0: A Cloud-Based Network of 3D Objects for Robust Grasp Planning Using a Multi-Armed Bandit Model with Correlated Rewards," presented at the IEEE Int. Conference on Robotics and Automation (ICRA), Stockholm, Sweeden, 2016.
[30] S.Liu and S.Carpin, "Kinematic Noise Propagation and Grasp Quality Evaluation," presented at the IEEE Int. Conference on Automation Science and Engineering (CASE), Fort Worth, TX, USA, 2016.
[31] M.P.Polverini, A.M.Zanchettin, S.Castello, and P.Rocco, "Sensorless and Constraint Based Peg-in-Hole Task Execution with a Dual-Arm Robot," presented at the ICRA, Stockholm, Sweden, 2016.
[32] H.Park, J.Park, D.-H.Lee, J.-H.Park, M.-H.Baeg, and J.-H.Bae, "Compliance-Based Robotic Peg-in-Hole Assembly Strategy Without Force Feedback," *IEEE Trans. Industrial Electronics,* vol. 64, no. 8, pp. 6299-6309, 2017.

[33] R.C.Luo, A.Chang, and Ch.Li, "A Novel Peg-in-Hole Approach based on Geometrical Analysis for Inclined Uncertainty," presented at the IEEE Int. Conf. on Advanced Intelligent Mechatronics (AIM), Munich, Germany, 2017.
[34] J.H.Su, R.Li, H.Qiao, J.Xu, Q.L.Ai, and J.K.Zhu, "Study on dual peg-in-hole insertion using of constraints formed in the environment," *Industrial Robot: An International Journal*, vol. 44, no. 6, pp. 730-740, 2017.
[35] K.Sharma, V.Shirwalkar, and P.K.Pal, "Peg-In-Hole search using convex optimization techniques," *Industrial Robot-an International Journal*, vol. 44, no. 5, pp. 618-628, 2017.
[36] J. M. Fitzpatrick, J. B. West, and C. R. Maurer, "Predicting Error in Rigid-Body Point-Based Registration," *IEEE Trans. Medical Imaging*, vol. 17, no. 5, pp. 694 -702, 1998.
[37] J. M. Fitzpatrick, "Fiducial registration error and target registration error are uncorrelated," in *SPIE Medical Imaging: Visualisation, Image-Guided Procedures and Modeling*, 2009, vol. 7261.
[38] M.W.Spong, S.Hutchinson, and M.Vidyasagar, *Robot Modeling and Control*. John Wiley & Sons, 2006.
[39] M.Franaszek and G.S.Cheok, "Improving Rigid-Body Registration Based on Points Affected by Bias and Noise," presented at the 8th Int. Precision Assembly Seminar, Chamonix, France, 2018.
[40] P. Bourke. (1999, 08/31/2016). *Interpolation methods*. Available: http://paulbourke.net/miscellaneous/interpolation/
[41] G.S.Cheok, M.Franaszek, K. V. Wyk, and J.A.Marvel, "Improving Automated Insertion Applications by Restoring Rigid-Body Condition in Point-Based Registration," National Institute of Standards and Technology Report NISTIR, vol. 8198, 2017.